In situ coarse-particle gold leaching from Witwatersrand ores using cyanide and glycine

by J.J. Mahumana[1], D. Groot[2], C. Adendorff[1], V. Notole[3,4], G.T. Nwaila[3]

Affiliation:
1 Milpark Business School, Milpark Education, Cape Town, South Africa.
2 Department of Civil, Mining and Process Engineering, Namibia University of Science and Technology, and Department of Materials Science and Metallurgical Engineering, University of Pretoria.
3 School of Geosciences, University of the Witwatersrand, South Africa.
4 School of Chemical and Metallurgical Engineering, University of the Witwatersrand, South Africa.

Correspondence to:
J.J. Mahumana

Email:
Joao.mahumane@gmail.com

Dates:
Received: 14 Apr. 2026
Revised: 10 Aug. 2026
Accepted: 30 Sep. 2026
Published: Oct. 2026

How to cite:
Mahumana J.J., Groot D., Adendorff C. Notole V., Nwaila G.T. 2026. In situ coarse-particle gold leaching from Witwatersrand ores using cyanide and glycine. *Journal of the Southern African Institute of Mining and Metallurgy*, vol. 126, no. 10, pp. 647 – 654

DOI ID:
https://doi.org/10.17159/2411-9717/3948/2026

ORCiD:
J.J. Mahumana
https://orcid.org/0009-0000-5787-5260
D. Groot
https://orcid.org/0000-0002-3235-5231
C. Adendorff
https://orcid.org/0000-0002-1520-9072
V. Notole
https://orcid.org/0000-0002-6624-9701
G.T. Nwaila
https://orcid.org/0000-0002-3974-9890

Abstract

In situ coarse-particle leaching could reduce surface disturbance relative to conventional mining, but its applicability to Witwatersrand conglomerates is poorly constrained. This study evaluates gold extraction from coarse (5 600 µm – 8 000 µm) Carbon Leader Middelvlei reef blends using cyanide and glycine under ambient bottle-roll conditions. Three blend ratios (7:3, 1:1, and 3:7; head grades 17 g/t – 32 g/t) were tested at pH 11 with 300 mg/L sodium cyanide or 1 500 mg/L glycine plus 1 500 mg/L potassium permanganate for 8 to 48 hours. Measured recovery remained low: the maximum 48 hour extraction was 15.3% for cyanide and 13.6% for glycine. In the Middelvlei-rich 3:7 blend, however, glycine provided faster early extraction (9.7% at 8 hours compared with 4.5% for cyanide). Glycine consumption (approximately 1.49 kg/t) was substantially higher than cyanide consumption (approximately 0.30 kg/t). Differences in matrix mineralogy, gold-grain compactness, and connected porosity provide plausible explanations for blend-dependent behaviour, but their individual effects were not isolated experimentally. The 48 hour endpoint was predefined for comparative screening of ore-property effects and early-stage kinetics, not for determination of maximum recovery. Accordingly, long-horizon model curves are presented only as unvalidated scenarios and do not establish an ultimate recovery or rate-limiting mechanism. Follow-up work will include at least one longer-duration experiment continued to a stable recovery plateau.

Keywords

in situ leaching, gold, glycine, cyanidation, ore blending, Witwatersrand Basin

Introduction

The Witwatersrand Basin in South Africa hosts the world's largest gold deposits and remains a major gold province (Frimmel, Nwaila, 2020). Gold is conventionally recovered by cyanidation, which forms stable, water-soluble gold complexes and can extract gold from low-grade ores (Hilson, Monhemius, 2006; Marsden, House, 2006). Although cyanidation is operationally mature, cyanide toxicity requires strict handling, detoxification, and disposal controls (Acheampong et al., 2010; Johnson, 2015; Liu et al., 2022). These constraints have motivated investigation of alternative lixiviants (Aylmore, 2016; Wang et al., 2021). Glycine is a biodegradable amino acid that can complex gold in alkaline media (Altinkaya et al., 2020; Eksteen et al., 2018; Jamett et al., 2023; Oraby et al., 2019, 2020), although glycine-only systems commonly require an oxidant and may exhibit slower overall extraction than cyanidation (Oraby, Eksteen, 2015).

In alkaline cyanide solutions, gold dissolves by oxidative complexation to dicyanoaurate. The overall stoichiometry is commonly represented by the Elsner reaction ($4Au + 8CN^- + O_2 + 2H_2O \rightarrow 4[Au(CN)_2]^- + 4OH^-$), so free cyanide concentration, dissolved oxygen, pH, and access to exposed gold surfaces control the leach response (Ilyas, 2018; Marsden, House, 2006). At pH 11, glycine is predominantly present as glycinate; an oxidant converts metallic gold to an oxidised state that is stabilised by gold–glycinate complexation. In the present tests, potassium permanganate supplied the oxidising capacity. Glycine leaching therefore depends on glycinate concentration, oxidant availability, alkalinity, competing base-metal reactions, and transport to exposed or connected gold surfaces. Because permanganate reduction products and gold–glycinate speciation vary with solution conditions, a single overall stoichiometric equation is not assumed for this system (Oraby, Eksteen, 2015; Oraby et al., 2020).

In situ leaching, in which lixiviants are introduced into a fractured ore zone and the pregnant solution is recovered, may reduce surface disturbance and material handling (Martens et al., 2021; Sinclair, Thompson, 2015; Steven, 2009). This study uses laboratory bottle-roll tests on coarse (5 600 µm – 8 000 µm) Carbon Leader Middelvlei reef blends as a comparative screening investigation. Its

primary objective is to link ore mineralogy, texture, gold-grain morphology, and blend composition to early-stage coarse-particle leaching by cyanide and glycine. The study does not attempt to establish maximum recovery within the 48 h experimental window; diffusion-type and logistic models are used only as exploratory descriptions of the measured trends and long-horizon scenarios.

Geological setting

The Archaean Witwatersrand Basin in northeastern South Africa forms part of the Kaapvaal Craton (Kröner et al., 2019), as illustrated in Figure 1. The succession is dominated by conglomerates, quartzites, shales, and minor volcanic units (Frimmel, Minter, 2002; Frimmel, 2019). The Witwatersrand Supergroup overlies a Palaeo to Mesoarchaean granitoid–greenstone basement and the Dominion Group, a bimodal volcanic succession with a thin basal siliciclastic unit (Armstrong et al., 1991; Marsh et al., 1989; Robb et al., 1992).

The Witwatersrand Supergroup is subdivided into the West Rand and Central Rand groups. The West Rand Group (approximately 5 150 m thick; 2.985 Ga – 2.914 Ga) records repeated marine transgressions and regressions and comprises quartzite, conglomerate, shale, iron formation, and the Crown Formation volcanic unit (Armstrong et al., 1991; Frimmel, Nwaila, 2020; Kositcin, Krapež, 2004; Nwaila et al., 2021). The Central Rand Group (approximately 2 880 m thick; 2.90 Ga – 2.79 Ga) is dominated by fluvial and fluvio-deltaic sandstone and conglomerate deposited in braidplain and alluvial-fan systems (Catuneanu, 2001; Els, 1998; Gumsley et al., 2020). Gold- and uranium-bearing conglomerates near the basin margins account for most historical production (Buck, Minter, 1985; Frimmel, 2019; Frimmel, Minter, 2002; Nwaila et al., 2017).

Prominent gold-bearing units in the Central Rand Group include the Carbon Leader and Middelvlei reefs. The Carbon Leader Reef rests on a palaeo-erosion surface at the base of the Main Formation (Fuchs et al., 2016), as presented in Figure 2. Gold grades range from approximately 3 g/t to more than 100 g/t, with the highest grades associated with carbon-seam facies (Frimmel, Nwaila, 2020). Gold occurs with pyrite, carbonaceous matter, and minor sulphides in a matrix containing muscovite, chlorite, chloritoid, and pyrophyllite between quartz and chert clasts (Da Costa, 2019; Da Costa et al., 2020; Frimmel, 2019; Fuchs, 2015; Nwaila et al., 2020; Zhao, 1998). These features have direct leaching implications: carbonaceous matter may adsorb dissolved gold complexes (preg-robbing), sulphides can consume oxidant or cyanide, phyllosilicate-rich matrix material can restrict connected porosity, and natural fractures can expose otherwise inaccessible gold and provide transport pathways (Fleming et al., 2011; Ilyas, 2018; Nwaila et al., 2020).

The Middelvlei Reef occurs approximately 60 m above the Carbon Leader reef (Jolly, 1984; Letanta, 2021; Nwaila et al., 2020), as can be observed in Figure 2. In the Carletonville area, it extends over more than 500 km² and comprises medium- to large-pebble oligomictic auriferous conglomerate interbedded with quartzite (Myers et al., 1993). The reef is typically 2 m – 4 m thick and contains thin pebble lags of approximately 10 cm (Letanta, 2021). Its gold grades are lower and more variable than those of the Carbon Leader reef, averaging approximately 5 g/t Au (Frimmel, Minter, 2002). Carbonaceous material is less abundant, and gold is commonly associated with quartz and pyrite (Els, 1987). The lower phyllosilicate and carbonaceous contents, higher quartz abundance, and fracture distribution provide testable contrasts in lixiviant penetration, oxidant demand, preg-robbing potential, and gold accessibility relative to the Carbon Leader reef.

Material and methods

Ore samples and preparation

Ore samples were collected underground from the Carbon Leader and Middelvlei reefs in Carletonville, South Africa, according to the sampling protocol used for the study. Approximately 80 kg of bulk material was obtained and dispatched to Super Laboratory Services (Johannesburg), the South African Nuclear Energy Corporation, and XRD Analytical & Consulting (Pretoria) for analysis. Samples were crushed into 5 600 µm – 8 000 µm, 1 700 µm – 5 600 µm, and

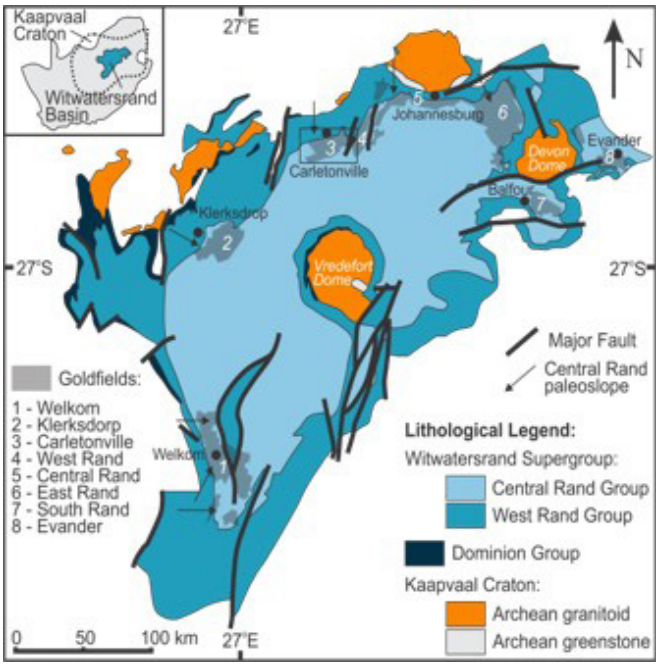

Figure 1—Location and simplified geological map of the Witwatersrand Basin and its major goldfields. The inset at upper left shows the location of the basin in South Africa; younger Ventersdorp and Transvaal cover successions have been removed (modified from Beukes et al., 2024; Frimmel et al., 2005)

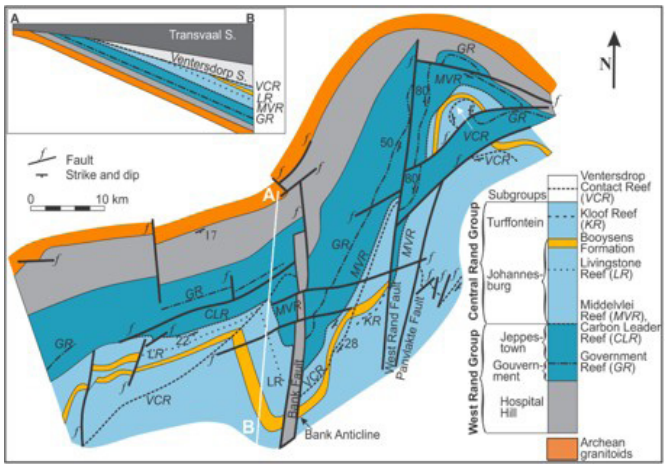

Figure 2—Simplified structural and stratigraphic relationships of the West Rand and Central Rand groups in the Carletonville goldfield. Younger Ventersdorp and Transvaal cover successions have been removed; the upper-left inset shows cross-section A–B, and the Ventersdorp Contact, Kloof, Middelvlei, Carbon Leader, and Government reefs are indicated

<1 700 µm fractions and blended at Carbon Leader:Middelvlei ratios of 30:70, 50:50, and 70:30. Subsamples were analysed by fire assay to determine head grades. The present manuscript reports the 5 600 µm – 8 000 µm fraction.

Micro X-ray computed tomography (micro-XCT)

Representative samples were scanned using a Nikon XTH 225L micro-XCT system at the South African Nuclear Energy Corporation to characterise three-dimensional mineral textures, fracture networks, and grain distributions (Bam et al., 2016, 2019; Becker et al., 2016). Samples were mounted, scanned at 80 kV, and reconstructed using CT Pro 3D and VG Studio Max 3.2. Mineral phases were segmented according to X-ray attenuation, enabling measurement of grain size, spatial distribution, morphology, and fracture connectivity relevant to lixiviant access.

X-ray powder diffraction (XRD)

Pulverised fractions were analysed using a Malvern Panalytical Aeris diffractometer with cobalt Kα radiation at XRD Analytical & Consulting. Diffractograms were interpreted using X'Pert HighScore Plus to identify crystalline phases; minor unindexed peaks were treated as trace components.

Bottle-roll leaching experiments

Triplicate bottle-roll tests were conducted for the ore blends. Slurries containing 30% solids were adjusted to pH 11 with lime and leached at ambient temperature (approximately 23 °C – 25 °C) using either 300 mg/L sodium cyanide or 1 500 mg/L glycine plus 1 500 mg/L potassium permanganate. Solution samples were collected after 8, 24, 32, and 48 h, and dissolved gold was measured by atomic absorption spectrometry. The 48 h endpoint was predefined for a comparative screening study intended to relate ore properties and blend composition to early-stage coarse-particle leaching; it was not selected to represent complete dissolution or maximum recovery. Tests were therefore terminated at 48 h even though recovery had not reached a plateau. Recovery at 8, 24, and 32 h was calculated relative to the measured 48 h-solution concentration and the independently determined 48 h recovery using Equation 1. At least one experiment continued until a stable recovery plateau is planned as follow-up validation.

$$Au\ recovery\ (\%)\ at\ t = \left(\frac{Au\ concentration\ at\ time\ t}{Final\ Au\ concentration}\right) \times Final\ Au\ recovery\ percentage \quad [1]$$

where t is the sampling time (8, 24, or 32 h), and "final" denotes the measured value at the 48 h study endpoint. Equation 1 assumes proportionality between dissolved gold concentration and recovery over the measured interval. The term "final" does not imply that maximum or equilibrium recovery was reached.

Modelling of leaching kinetics

A diffusion-type expression was fitted to evaluate the sensitivity of recovery to particle radius and effective internal transport (Crank, 1979), as per Equation 2. A logistic curve was also fitted to the glycine data as an upper-bound scenario, as per Equation 3. For that scenario, the carrying capacity was fixed at 100% and the growth rate and inflection time were fitted using SciPy. Fixing the carrying capacity at 100% imposes a mathematical upper bound; it is not an estimate of experimentally achievable recovery. Both models assume idealised particle geometry and transport, and neither was validated beyond the 48 h experimental window. The fitted parameters are therefore used only to compare measured early-stage trends and illustrate extrapolation uncertainty, not to determine the true recovery limit or rate-limiting mechanism.

$$C_{(t)} = C_0\left(1 - \left(1 + \frac{4Dt}{R^2}\right)^{-0.5}\right) \quad [2]$$

where C_t is cumulative recovery (%) at time t, D is the effective diffusion coefficient, R is particle radius, and C_0 is the fitted asymptotic recovery parameter (%). Equation 2 represents increasing diffusion resistance with particle size and assumes spherical particles, uniform internal transport, and no convective contribution. These assumptions do not reproduce the irregular particle shapes, surface roughness, and fracture networks observed by micro-XCT.

$$f(t) = \frac{K}{1+e^{-r(t-t_0)}} \quad [3]$$

where $f(t)$ is cumulative recovery (%), K is the carrying capacity, r is the intrinsic growth rate, and t_0 is the inflection time. In the scenario shown, K was fixed at 100% solely to define an upper-bound curve. Because the fit does not use observations beyond 48 h and has no long-duration validation, the fitted parameters must not be interpreted as a measured maximum recovery or a confirmed rate-limiting mechanism.

Results

Ore mineralogy and characteristics

The Carbon Leader reef (CLR) is a well-sorted, auriferous, clast- and matrix-supported conglomerate. Subrounded quartz clasts (0.2 mm – 10 mm) as shown in Figures 3a – c, occur in a fine-grained matrix (<0.4 mm) containing muscovite, chlorite, chloritoid, and pyrophyllite. Pyrite grains (0.02 mm – 0.5 mm) are concentrated in matrix interstices and locally form stringers approximately 2 mm wide. Trace phases include carbonaceous matter, uranium-bearing minerals, pentlandite, and visible gold. The Middelvlei reef (MVR) is also a well-sorted quartz-pebble conglomerate, as illustrated in Figures 3d – f, but its matrix contains less muscovite and pyrophyllite. Quartz- and calcite-filled fractures occur in both ores. Quantitative X-ray diffraction shows that the CLR samples average 86.7 wt.% quartz, 6.0 wt.% muscovite, 2.5 wt.% pyrophyllite, 2.4 wt.% chloritoid, and 2.4 wt.% pyrite, whereas the MVR samples average 96.8 wt.% quartz, 0.8 wt.% muscovite, 0.5 wt.% pyrophyllite, and 2.1 wt.% pyrite, with trace kaolinite, as per Table 1. Thus, the ores have similar pyrite contents but differ substantially in quartz

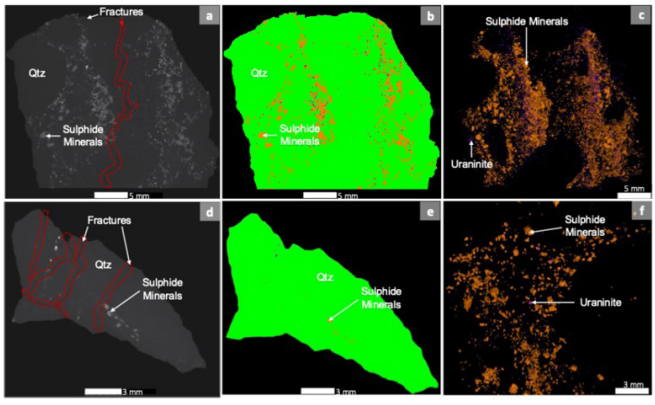

Figure 3—Ore mineralogy and textures of the Carbon Leader reef (a–c) and Middelvlei reef (d–f) imaged by micro-XCT. In panels b and e, green denotes silicate minerals (predominantly quartz), orange denotes sulphide minerals (predominantly pyrite), and purple denotes uraninite

and phyllosilicate abundance, which may affect oxidant demand, pore connectivity, surface coatings, and access to gold.

Micro-XCT analysis characterised gold-grain morphology (Figures 4 and 5). CLR gold grains ranged from 0.01 mm to 0.5 mm (n = 1 813), with mean compactness of 0.47 and mean sphericity of 0.66 (Figure 4b). MVR gold grains ranged from 0.02 mm to 0.7 mm (n = 1 004), with mean compactness of 0.62 and mean sphericity of 0.72 (Figure 4a). The absolute difference in compactness (0.15) is greater than the difference in sphericity (0.06). These descriptors were not varied independently, so they cannot be assigned a causal effect on leaching. The larger compactness contrast, together with the measured matrix-mineralogy differences, provides a more plausible hypothesis for blend-dependent accessibility than sphericity alone.

Table 1

Mineral contents determined by X-ray diffraction for selected Carbon Leader reef (CLR) and Middelvlei reef (MVR) samples; values are in wt.%

Sample	CLR 1	CLR 2	MVR 1	MVR 2
Quartz	81.7	91.7	96.8	96.7
Pyrite	2.2	2.6	2.1	2.0
Muscovite	7.1	4.9	0.6	0.9
Pyrophyllite	4.2	0.8	0.5	0.5
Kaolinite	0	0	trace	trace
Chloritoid	4.8	0	0	0

Coarse-particle leaching

The 5 600 µm – 8 000 µm fraction was leached with cyanide and glycine at CLR:MVR blend ratios of 7:3, 1:1, and 3:7 (as per Figures 6a and b and Tables 2 to 3). Extraction was low for both lixiviants. At 48 h, cyanide recovery was 12.63%, 13.09%, and 15.28% for the 7:3, 1:1, and 3:7 blends, respectively, compared with 10.88%, 9.98%, and 13.63% for glycine. Glycine produced faster 8 h extraction in the 1:1 and 3:7 blends (6.04% and 9.70%, respectively) than cyanide (4.35% and 4.52%), whereas the 7:3 blend gave similar 8 h values (5.23% for glycine and 5.57% for cyanide). Cyanide therefore provided higher 48 h recovery in all three blends, while glycine provided faster early extraction only in the blends containing at least 50% MVR. Maximum measured reagent consumption was approximately 0.31 kg/t for cyanide and 1.49 kg/t for glycine (Figures 6c and d). These data demonstrate measurable coarse-particle extraction but do not support describing either system as efficient at the tested contact time.

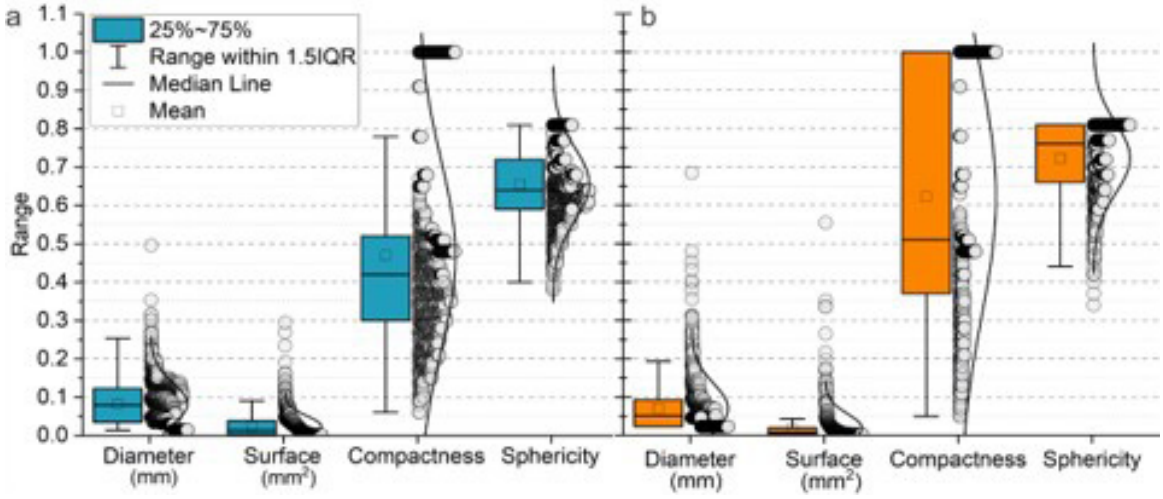

Figure 4—Box-and-density plots of gold-grain diameter, surface area, compactness, and sphericity for (a) the Middelvlei reef and (b) the Carbon Leader reef, determined by micro-XCT. The datasets contain 1 004 and 1 813 grains, respectively; IQR denotes interquartile range

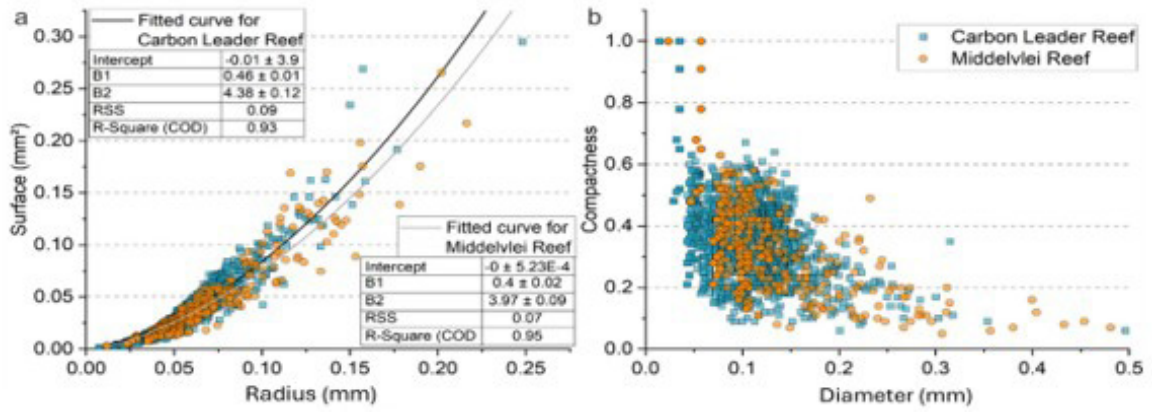

Figure 5—Micro-XCT gold-grain relationships for the Carbon Leader and Middelvlei reefs: (a) radius versus surface area with quadratic fits, y = intercept + B_1x + B_2x^2, and (b) diameter versus compactness; RSS denotes residual sum of squares

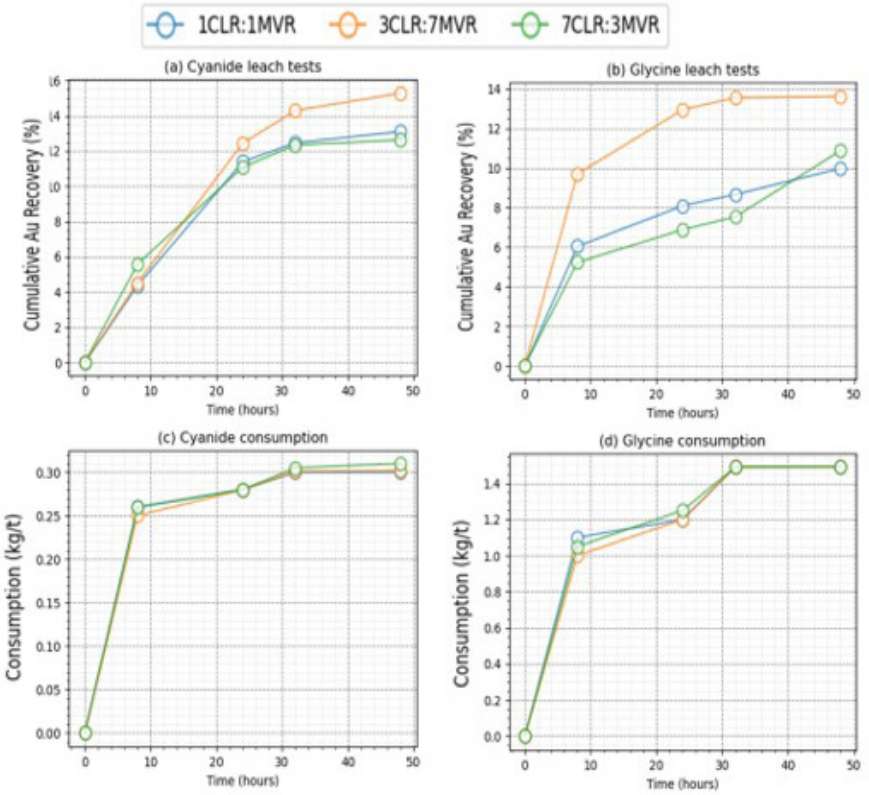

Figure 6—Measured gold recovery during (a) cyanide and (b) glycine leaching of Carbon Leader reef (CLR)–Middelvlei reef (MVR) blends, with corresponding consumption of (c) cyanide and (d) glycine

Table 3
Coarse-particle gold leaching with glycine; reagent consumption and recovery are reported

Ore blend	Time (h)	pH	Glycine consumed (kg/t)	Au in solution (mg/L)	Au recovery (%)
7CLR:3MVR	0	8.8	0.00	0	0.00
7CLR:3MVR	8	10.7	1.05	1.36	5.23
7CLR:3MVR	24	10.7	1.25	1.79	6.88
7CLR:3MVR	32	10.7	1.49	1.96	7.54
7CLR:3MVR	48	10.7	1.49	2.83	10.88
1CLR:1MVR	0	8.9	0.00	0	0.00
1CLR:1MVR	8	10.8	1.10	1.15	6.04
1CLR:1MVR	24	10.8	1.20	1.54	8.09
1CLR:1MVR	32	10.8	1.49	1.65	8.67
1CLR:1MVR	48	10.8	1.49	1.90	9.98
3CLR:7MVR	0	8.8	0.00	0	0.00
3CLR:7MVR	8	10.8	1.00	1.43	9.70
3CLR:7MVR	24	10.8	1.20	1.91	12.95
3CLR:7MVR	32	10.8	1.49	2.00	13.56

Table 2
Coarse-particle gold leaching with cyanide

Ore blend	Time (h)	pH	Cyanide consumed (kg/t)	Au in solution (mg/L)	Au recovery (%)
7CLR:3MVR	0	8.8	0.00	0	0.00
7CLR:3MVR	8	10.7	0.26	1.50	5.57
7CLR:3MVR	24	10.7	0.28	2.98	11.07
7CLR:3MVR	32	10.7	0.305	3.32	12.33
7CLR:3MVR	48	10.7	0.31	3.40	12.63
1CLR:1MVR	0	8.9	0.00	0	0.00
1CLR:1MVR	8	10.8	0.26	0.89	4.35
1CLR:1MVR	24	10.8	0.28	2.33	11.38
1CLR:1MVR	32	10.8	0.3	2.55	12.46
1CLR:1MVR	48	10.8	0.3	2.68	13.09
3CLR:7MVR	0	8.9	0.00	0	0.00
3CLR:7MVR	8	10.8	0.25	0.68	4.52
3CLR:7MVR	24	10.8	0.28	1.87	12.42
3CLR:7MVR	32	10.8	0.301	2.15	14.28
3CLR:7MVR	48	10.8	0.302	2.30	15.28

Exploratory logistic-growth simulations

Figure 7 shows logistic curves extrapolated to 400 h for the glycine tests. Because the carrying capacity was fixed at 100%, the curves approach 90% – 97% recovery by approximately 200 h. These values are a mathematical consequence of the imposed upper bound and

the fitted growth parameters; they are not experimental evidence of near-complete recovery. Only four non-zero observations were available up to 48 h, and no test was continued to a plateau. The extrapolations are therefore non-unique and cannot identify the true recovery limit or rate-limiting step. Possible mechanisms for later exposure—diffusion through connected pores, access along existing or newly opened microfractures, and slow dissolution of partly exposed grains—were not measured in this study and remain hypotheses. The curves are retained only to illustrate extrapolation uncertainty and to motivate a follow-up experiment continued until recovery stabilises.

Discussion

The ore-characterisation data identify several plausible controls on coarse-particle leaching, but they do not isolate any single causal variable. CLR and MVR have similar mean pyrite contents (approximately 2.4 wt.% and 2.1 wt.%, respectively), but their overall mineralogy is not similar: CLR contains markedly more muscovite, pyrophyllite, and chloritoid, whereas MVR contains approximately 10 percentage points more quartz. The compactness means differ by 0.15, compared with a sphericity difference of only 0.06. Accordingly, the larger compactness contrast and the phyllosilicate-rich CLR matrix are more credible contributors to differences in connected porosity and surface accessibility than sphericity alone. Carbonaceous matter may also promote preg-robbing, and pyrite or other reactive phases may consume oxidant or cyanide (Fleming et al., 2011; Ilyas, 2018). These effects were not tested independently and are presented as mechanisms for future validation rather than demonstrated causes.

The kinetic comparison is blend- and time-dependent. Glycine gave higher 8 h recovery than cyanide for the 1:1 blend (6.04% compared with 4.35%) and the 3:7 blend (9.70% compared with 4.52%), but not for the CLR-rich 7:3 blend (5.23% compared with 5.57%). By 48 h, cyanide recovery exceeded glycine recovery for every blend: 12.63% compared with 10.88% for 7:3, 13.09% compared with 9.98% for 1:1, and 15.28% compared with 13.63% for 3:7. Cyanide also required substantially less reagent on a mass basis (approximately 0.30 kg/t compared with 1.49 kg/t glycine). It is therefore inaccurate to describe cyanide as having universally faster kinetics or glycine as giving comparable final extraction. The data instead show faster initial glycine extraction in MVR-rich blends, followed by higher 48 h cyanide recovery in all blends.

The trials were terminated at the predefined 48 h screening endpoint before maximum recovery was reached. This design was suitable for the primary objective of linking ore properties and blend composition to early-stage leaching of 5.6 mm – 8.0 mm particles, but it cannot establish the ultimate recovery or controlling mechanism. The diffusion-type and logistic fits should therefore be viewed as descriptive and scenario-based, respectively. In particular, fixing logistic carrying capacity at 100% precludes using the fitted curve as validation of near-complete extraction. A follow-up study will include at least one longer-duration test continued until successive measurements show a stable plateau, with reagent residuals and solution chemistry monitored to distinguish transport limitation from reagent depletion or passivation. Subsequent work may also evaluate controlled fracture enhancement or flow stimulation to test whether increased connected surface area improves coarse-particle recovery.

Conclusion

Cyanide and glycine produced measurable but low gold extraction from 5.6 mm – 8.0 mm Witwatersrand ore particles. After 48 h, cyanide recovery was 12.63% – 15.28%, compared with 9.98% – 13.63% for glycine. Glycine showed faster initial extraction in the 1:1 and 3:7 blends, but lower 48 h recovery, and its consumption was approximately five times that of cyanide on a mass-per-tonne basis. Ore characterisation showed similar pyrite contents but substantial differences in quartz and phyllosilicate abundance; the compactness contrast also exceeded the sphericity contrast. These associations plausibly explain blend-dependent accessibility, but causality was not established. The predefined 48 h endpoint was designed to link ore properties to early-stage coarse-particle leaching, not to determine maximum recovery. Long-horizon model curves remain unvalidated scenarios. Follow-up work will include at least one longer-duration test continued to a stable recovery plateau, with monitoring to distinguish diffusion, reagent depletion, passivation, and fracture-controlled access.

References

Acheampong, M.A., Meulepas, R.J.W., Lens, P.N.L. 2010. Removal of heavy metals and cyanide from gold mine wastewater. Journal of Chemical Technology & Biotechnology, vol. 85, no. 5, pp. 590–613. https://doi.org/10.1002/jctb.2358

Altinkaya, P., Wang, Z., Korolev, I., Hamuyuni, J., Haapalainen, M.,

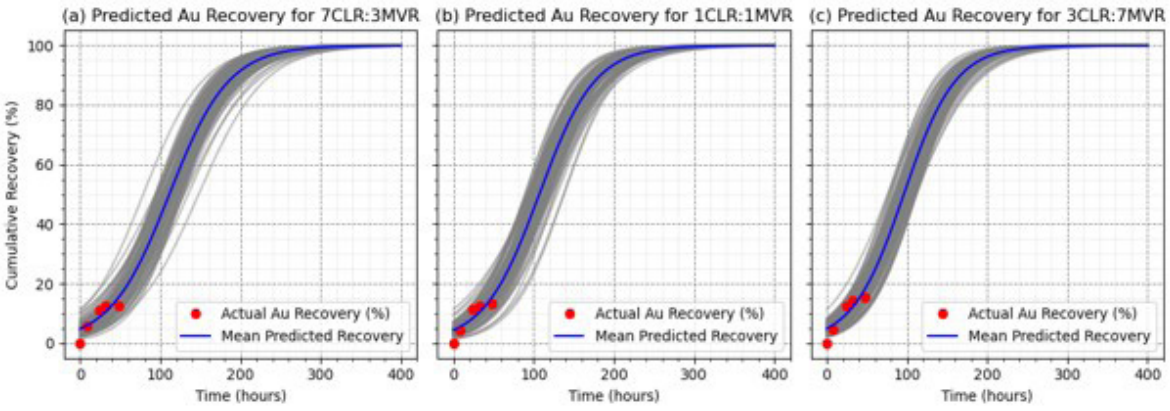

Figure 7—Unvalidated upper-bound logistic scenarios (grey curves) for glycine leaching of CLR:MVR blends of (a) 7:3, (b) 1:1, and (c) 3:7; red points are the measured data through 48 h. The 100% carrying capacity was imposed and is not an experimentally determined recovery limit

Kolehmainen, E., Yliniemi, K., Lundström, M. 2020. Leaching and recovery of gold from ore in cyanide-free glycine media. *Minerals Engineering*, vol. 158, article 106610.

Armstrong, R.A., Compston, W., Retief, E.A., Williams, I.T., Welke, H.J. 1991. Zircon ion microprobe studies bearing on the age and evolution of the Witwatersrand triad. *Precambrian Research*, vol. 53, nos. 3–4, pp. 243–266.

Aylmore, M.G. 2016. Alternative lixiviants to cyanide for leaching gold ores. Advances in Gold Ore Processing. 2nd ed. Adams, M.D. (ed.). Elsevier.

Bam, L.C., Miller, J.A., Becker, M., Basson, I.J. 2019. X-ray computed tomography: Practical evaluation of beam hardening in iron ore samples. *Minerals Engineering*, vol. 131, pp. 206–215.

Bam, L.C., Miller, J.A., Becker, M., De Beer, F.C., Basson, I. 2016. X-ray computed tomography—determination of rapid scanning parameters for geometallurgical analysis of iron ore. See AusIMM (2016), pp. 209–219.

Becker, M., Jardine, M.A., Miller, J.A., Harris, M. 2016. X-ray computed tomography: A geometallurgical tool for three-dimensional textural analysis of drill core. See AusIMM (2016), pp. 231–240.

Beukes, N.J., Guy, B.M., Thiele, S.T. 2024. Stratigraphy and basin analysis of the West Rand Group, Witwatersrand Supergroup. *South African Journal of Geology*, vol. 127, no. 2, pp. 239–270.

Buck, S.G., Minter, W.E.L. 1985. Placer formation by fluvial degradation of an alluvial fan sequence: The Proterozoic Carbon Leader placer, Witwatersrand Supergroup, South Africa. *Journal of the Geological Society*, vol. 142, no. 5, pp. 757–764.

Catuneanu, O. 2001. Flexural partitioning of the late Archaean Witwatersrand foreland system, South Africa. *Sedimentary Geology*, vol. 141, pp. 95–112.

Crank, J. 1979. The Mathematics of Diffusion. 2nd ed. Oxford University Press, Oxford, UK.

Da Costa, G., Hofmann, A., Agangi, A. 2020. A revised classification scheme of pyrite in the Witwatersrand Basin and application to placer gold deposits. *Earth-Science Reviews*, vol. 201, article 103064. https://doi.org/10.1016/j.earscirev.2019.103064

Da Costa, G.V. 2019. Evaluation of syngenetic gold deposition in syn-sedimentary pyrite of the Witwatersrand Basin. Thesis, University of Johannesburg, South Africa.

Eksteen, J.J., Oraby, E.A., Tanda, B.C., Tauetsile, P.J., Bezuidenhout, G.A., Newton, T., Trask, F., Bryan, I. 2018. Towards industrial implementation of glycine-based leach and adsorption technologies for gold–copper ores. *Canadian Metallurgical Quarterly*, vol. 57, no. 4, pp. 390–398.

Els, B.G. 1987. The auriferous Middelvlei Reef depositional system, West Wits Line, Witwatersrand Supergroup. Thesis, University of Johannesburg, South Africa.

Els, B.G. 1998. The auriferous late Archaean sedimentation systems of South Africa: Unique palaeo-environmental conditions. *Sedimentary Geology*, vol. 120, no. 1–4, pp. 205–224.

Fleming, C.A., Mezei, A., Bourricaudy, E., Canizares, M., Ashbury, M. 2011. Factors influencing the rate of gold cyanide leaching and adsorption on activated carbon, and their impact on the design of CIL and CIP circuits. Minerals Engineering, vol. 24, no. 6, pp. 484–494.

Frimmel, H.E. 2019. The Witwatersrand Basin and its gold deposits. The Archaean Geology of the Kaapvaal Craton, Southern Africa, pp. 255–275.

Frimmel, H.E., Minter, W.E.L. 2002. Recent developments concerning the geological history and genesis of the Witwatersrand gold deposits, South Africa. *Society of Economic Geologists Special Publication*, vol. 9, pp. 17–45.

Frimmel, H.E., Nwaila, G.T. 2020. Geologic evidence of syngenetic gold in the Witwatersrand Goldfields. DOI: 10.5382/SP.23.31

Frimmel, H.E., Groves, D.I., Kirk, J., Ruiz, J., Chesley, J., Minter, W.E.L. 2005. The formation and preservation of the Witwatersrand goldfields, the largest gold province in the world. Economic Geology One Hundredth Anniversary Volume. Hedenquist, J.W., Thomson, J.F.H., and Goldfarb, R.J. (eds.). *Society of Economic Geologists, Littleton*, CO, USA. pp. 769–797.

Fuchs, S. 2015. The role of hydrocarbons in the Witwatersrand gold and uranium deposits, and the genesis of Witwatersrand-style Black Reef deposits, South Africa. Thesis, McGill University, Canada.

Fuchs, S., Williams-Jones, A.E., Jackson, S.E., Przybylowicz, W.J. 2016. Metal distribution in pyrobitumen of the Carbon Leader Reef, Witwatersrand Supergroup, South Africa: Evidence for liquid hydrocarbon ore fluids. *Chemical Geology,* vol. 426, pp. 45–59.

Gumsley, A., Stamsnijder, J., Larsson, E., Söderlund, U., Naeraa, T., De Kock, M., Sałacińska, A., Gawęda, A., Humbert, F., Ernst, R. 2020. Neoarchaean large igneous provinces on the Kaapvaal Craton in southern Africa redefine the formation of the Ventersdorp Supergroup and its temporal equivalents. Bulletin, vol. 132, no. 9–10, pp. 1829–1844.

Hilson, G., and Monhemius, A.J. 2006. Alternatives to cyanide in the gold mining industry: What prospects for the future? *Journal of Cleaner Production*, vol. 14, nos. 12–13, pp. 1158–1167. https://doi.org/10.1016/j.jclepro.2004.09.005

Ilyas, S. 2018. Cyanidation of gold-bearing ores. *Gold Metallurgy and the Environment*, pp. 51–102. CRC Press.

Jamett, I., Carrasco, P., Olmos, M., Hernández, P. 2023. Glycine/glutamate: "Green" alternatives to recover metals from minerals/residues—review of current research. *Minerals*, vol. 13, no. 1, article 22. https://doi.org/10.3390/min13010022

Johnson, C.A. 2015. The fate of cyanide in leach wastes at gold mines: An environmental perspective. *Applied Geochemistry*, vol. 57, pp. 194–205. https://doi.org/10.1016/j.apgeochem.2014.05.023

Jolly, M.K. 1984. The sedimentology and economic potential of the auriferous Middelvlei Reef on Driefontein Consolidated Limited. Thesis, University of Johannesburg, South Africa.

Kositcin, N., Krapež, B. 2004. Relationship between detrital zircon age spectra and the tectonic evolution of the Late Archaean Witwatersrand Basin, South Africa. *Precambrian Research*, vol. 129, nos. 1–2, pp. 141–168.

Kröner, A., Hoffmann, J.E., Wong, J.M., Geng, H.Y., Schneider, K.P., Xie, H., Yang, J.H., Nhleko, N. 2019. Archaean crystalline rocks of the eastern Kaapvaal Craton. The Archaean Geology of the Kaapvaal Craton, Southern Africa, pp. 1–32.

Letanta, D. 2021. Application of sedimentological and gold-assay data for resource estimation: A case study of the Middelvlei Reef, Witwatersrand Basin, South Africa. PhD thesis, University of the Witwatersrand, South Africa.

Liu, Z.W., Guo, X.Y., Tian, Q.H., Zhang, L. 2022. A systematic review of gold extraction: Fundamentals, advancements, and challenges toward alternative lixiviants. *Journal of Hazardous Materials*, vol. 440, article 129778.

Marsden, J., House, I. 2006. The Chemistry of Gold Extraction. 2nd ed. Society for Mining, Metallurgy, and Exploration, USA.

Marsh, J.S., Bowen, M.P., Rogers, N.W., Bowen, T.B. 1989. Volcanic rocks of the Witwatersrand Triad, South Africa. II: Petrogenesis of mafic and felsic rocks of the Dominion Group. *Precambrian Research*, vol. 44, no. 1, pp. 39–65.

Martens, E., Prommer, H., Sprocati, R., Sun, J., Dai, X., Crane, R., Jamieson, J., Tong, P.O., Rolle, M., Fourie, A. 2021. Toward a more sustainable mining future with electrokinetic in situ leaching. *Science Advances,* vol. 7, no. 18, article eabf9971.

Myers, R.E., Zhou, T., Phillips, G.N. 1993. Sulphidation in the Witwatersrand Goldfields: Evidence from the Middelvlei Reef. *Mineralogical Magazine*, vol. 57, no. 388, pp. 395–405. https://doi.org/10.1180/minmag.1993.057.388.04

Nwaila, G., Frimmel, H.E., Minter, W.E. 2017. Provenance and geochemical variations in shales of the Mesoarchaean Witwatersrand Supergroup. *Journal of Geology*, vol. 125, no. 4, pp. 399–422.

Nwaila, G.T., Bourdeau, J.E., Jinnah, Z., Frimmel, H.E., Bybee, G.M., Zhang, S.E., Manzi, M.S.D., Minter, W.E.L., Mashaba, D. 2021. The significance of erosion channels on gold metallogeny in the Witwatersrand Basin (South Africa): Evidence from the Carbon Leader Reef in the Carletonville goldfield. *Economic Geology*, vol. 116, no. 2, pp. 265–284.

Nwaila, G.T., Ghorbani, Y., Becker, M., Frimmel, H.E., Petersen, J., Zhang, S. 2020. Geometallurgical approach for implications of ore blending on cyanide leaching and adsorption behaviour of Witwatersrand gold ores, South Africa. *Natural Resources Research*, vol. 29, pp. 1007–1030.

Oraby, E.A., Eksteen, J.J. 2015. The leaching of gold, silver, and their alloys in alkaline glycine–peroxide solutions and their adsorption on carbon. *Hydrometallurgy*, vol. 152, pp. 199–203. https://doi.org/10.1016/j.hydromet.2014.12.015

Oraby, E.A., Eksteen, J.J., Karrech, A., Attar, M. 2019. Gold extraction from palaeochannel ores using an aerated alkaline glycine lixiviant for consideration in heap and in situ leaching applications. *Minerals Engineering*, vol. 138, pp. 112–118.

Oraby, E.A., Eksteen, J.J., O'Connor, G.M. 2020. Gold leaching from oxide ores in alkaline glycine solutions in the presence of permanganate. Hydrometallurgy, vol. 198, article 105527. https://doi.org/10.1016/j.hydromet.2020.105527

Robb, L.J., Davis, D.W., Kamo, S.L., Meyer, F.M. 1992. Ages of altered granites adjoining the Witwatersrand Basin with implications for the origin of gold and uranium. *Nature*, vol. 357, no. 6380, pp. 677–680.

Sinclair, L., Thompson, J. 2015. In situ leaching of copper: Challenges and future prospects. *Hydrometallurgy*, vol. 157, pp. 306–324.

Steven, N. 2009. Potential in situ leach exploitation of backfilled Witwatersrand gold mines: Parameters and flow-rate calculations from a Zambian Copperbelt analogue. Proceedings of the World Gold Conference. *Southern African Institute of Mining and Metallurgy, Johannesburg*. pp. 193–196.

Wang, J., Faraji, F., Ramsay, J., Ghahreman, A. 2021. A review of biocyanidation as a sustainable route for gold recovery from primary and secondary low-grade resources. *Journal of Cleaner Production*, vol. 296, article 126457.

Zhao, B. 1998. A mineralogical and geochemical study of alteration associated with the Ventersdorp Contact Reef in the Witwatersrand Basin, South Africa. PhD thesis, Wits University, South Africa. ◆

